

NACA RM E52F02

NACA

TECH LIBRARY KAFB, NM  
0143418

# RESEARCH MEMORANDUM

TRANSONIC FREE-FLIGHT INVESTIGATION OF THE TOTAL DRAG  
AND OF THE COMPONENT DRAGS (COWL PRESSURE, ADDITIVE,  
BASE, FRICTION, AND INTERNAL) ENCOUNTERED BY A  
16-INCH-DIAMETER RAM-JET ENGINE FOR MACH  
NUMBERS FROM 0.80 TO 1.43

By Wesley E. Messing and Leonard Rabb

Lewis Flight Propulsion Laboratory  
Cleveland, Ohio

NATIONAL ADVISORY COMMITTEE  
FOR AERONAUTICS

WASHINGTON

August 13, 1952

6746

5-2-52/13



1G

NACA RM E52F02

~~CONFIDENTIAL~~

## NATIONAL ADVISORY COMMITTEE FOR AERONAUTICS

RESEARCH MEMORANDUM

TRANSONIC FREE-FLIGHT INVESTIGATION OF THE TOTAL DRAG AND OF THE

COMPONENT DRAGS (COWL PRESSURE, ADDITIVE, BASE, FRICTION, AND

INTERNAL) ENCOUNTERED BY A 16-INCH-DIAMETER RAM-JET

ENGINE FOR MACH NUMBERS FROM 0.80 to 1.43

By Wesley E. Messing and Leonard Rabb

## SUMMARY

A free-flight investigation of the drag on four full-scale models of 16-inch-diameter ram-jet engines was conducted. For each model, the total, base, internal, and external drag were evaluated. Data obtained from one model were sufficient that the constituents of the external drag, namely, cowl pressure, additive, and friction drags, could be evaluated for a Mach number range from 0.80 to 1.43 and a mass-flow ratio from 0.66 to 0.84. The drag results from this model are presented herein, and a general comparison is made with the data obtained from three other models. The model was launched from an airplane at 35,000 feet, rocket-propelled to supersonic velocities during the free fall, and then decelerated because of its drag through the transonic range before impact. Thus data were obtained over the same Mach number range for rocket-on and rocket-off operation.

It was possible to account for at least 94 percent of the total drag, as determined directly from accelerometer data, by summation of the constituent drags, that is, cowl pressure, additive, friction, base, and internal drag, each of which was determined independently from pressure measurements. A net thrust force was encountered acting on the cowl at Mach numbers less than 1.22 and 1.39 for the rocket-off and rocket-on conditions, respectively. For the rocket-off condition the external drag coefficient, excluding base drag, had a minimum value of 0.13 at a Mach number of 0.90 and gradually increased to a maximum value of 0.20 at a Mach number of 1.30. This compares with a total drag coefficient variation from 0.44 at a Mach number of 0.90 to 0.62 at a Mach number of 1.15. Good agreement was obtained between the predicted ( $1/7$  power law) and experimental boundary-layer velocity profiles at radial distances from the body in excess of 20 percent of the boundary-layer thickness. Below this value the experimental data deviated slightly from the predicted values.

2549

## INTRODUCTION

In order to predict the performance of ram-jet engines operating in the transonic speed range, it is necessary to estimate reliably the propulsive (thrust minus drag) forces. At the present time, the internal thrust of the engine may be readily predicted, but it is extremely difficult to estimate the transonic drag because existing theories are inadequate and little experimental information is available. As a result, an experimental investigation employing the free-flight drop technique was conducted by the NACA Lewis Laboratory utilizing the facilities of the NACA Langley Pilotless Aircraft Research Station, Wallops Island, Virginia. The purpose of this investigation was to evaluate the transonic drag encountered with a 16-inch-diameter ram-jet engine. Four full-scale models were dropped from an F-82 airplane (fig. 1) at a pressure altitude of 35,000 feet, rocket-propelled to supersonic velocities, and then decelerated through the transonic range before impact. The models were lightweight facsimiles of the NACA 16-C-type ram-jet engine (reference 1) which was designed to operate with a normal shock at the inlet at a free-stream Mach number of 1.60. The 50° spike of the centerbody was so positioned that the attached conical shock would intercept the lip of the outer shell at a free-stream Mach number of 1.80. An annular restriction was inserted in the outlet of each model to reduce the internal air flow to representative subcritical inlet mass flows encountered during combustion. Data were obtained at several inlet mass-flow ratios and outlet pressure ratios by using a different outlet area in each model. These data were recorded by radio-telemetry and radar-tracking equipment on continuous records.

The total, base, internal, and external drag of the first two models investigated are reported in reference 2. Similar data were obtained from a third model. However, in the fourth model investigated, the instrumentation was increased from 10 to 30 measurements so that the constituents of the external drag, namely, the additive, cowl pressure, and friction drag, could be determined. The drag results of this model over a free-stream Mach number range from 0.8 to 1.43 are presented herein and are compared with the results obtained from the other three models. In the presentation of the data it is convenient to refer to rocket-off and rocket-on operation because at a given free-stream Mach number, the operation of the rocket altered the mass flow through the engine, which had a subsequent effect on the over-all drag characteristics of the engine.

## SYMBOLS

The following symbols are used in this report:

$a_n$  net acceleration, ft/sec<sup>2</sup>

2549

$C_D$  drag coefficient,  $D/q_0 S_m$

$C_F$  rocket thrust coefficient,  $T/q_0 S_m$

$C_F$  friction drag coefficient based on wetted area upstream of boundary-layer survey rake, 44.36 sq ft

$C_T$  propulsive thrust coefficient,  $(T-D)/q_0 S_m$

$D$  drag, lb

$d$  distance downstream of cowl lip, in.

$M$  Mach number

$m$  mass flow, lb/sec

$m_0$  mass flow in free-stream tube equal in area to projected lip area of cowl, lb/sec

$P$  total pressure, lb/sq ft abs

$p$  static pressure, lb/sq ft abs

$\Delta p$  pitot static position error, lb/sq ft

$q$  dynamic pressure, lb/sq ft ( $0.7 pM^2$ )

$Re$  Reynolds number based on model length of 14.3 feet

$r$  radial distance from axis of symmetry, in.

$S_m$  maximum cross-sectional area, 1.4 sq ft

$T$  thrust, lb

$t$  static temperature,  $^{\circ}R$

$V_\delta$  velocity at boundary-layer thickness  $\delta$ , ft/sec

$v_l$  local velocity in boundary layer, ft/sec

$x$  distance downstream of apex of central body, in.

$y$  radial distance from external surface of shell, in.

- 8 boundary-layer thickness, in.
- θ angular displacement from center line of base pressure orifices,  
as shown in figure 2, deg

Subscripts:

- a additive
- b base
- c cowl
- f friction
- i internal
- l local conditions
- s spike
- t total
- 0 station at free stream
- 1 station at cowl inlet
- 2 station at diffuser outlet
- 3 station at model outlet

2549

#### APPARATUS AND PROCEDURE

A schematic diagram including dimensions and the location of the instrumentation pickups for model 4 is shown in figure 2. Coordinates of the inlet of the ram-jet engine are included in figure 3. A self-averaging total-head probe was used in order to obtain an adequate total-pressure survey at the inlet with only a single measurement. Ground tests indicated good agreement between the data from this probe and the average total pressure as obtained from a 10-tube survey rake. The probe, as shown in figure 4, has a slotted intake, the sides of which are radial lines, thus making any segment of the rake intake area a function of the flow area covered by that segment. Included in figure 4 is a sketch of the boundary-layer survey rake. The material in reference 2 in regard to APPARATUS AND PROCEDURE applies to model 4 with the addition of the following information: Model 4 contained a 10-channel telemetering system which incorporated an NACA-designed

switching unit so that 30 independent measurements would be transmitted within a 0.17-second time interval. A photograph of the centerbody (fig. 5) illustrates the general arrangement of the telemetering equipment. Included in figure 5 is a tabulated listing of the instrumentation giving the location, range, and frequency of each instrument.

Model 4 was released at a pressure altitude of 35,000 feet and a free-stream Mach number of 0.55. Rocket ignition occurred approximately 13 seconds after release. At the end of the 14-second rocket-boost period, the rocket thrust and the force of gravity had accelerated the model to a maximum Mach number of 1.43 at a pressure altitude of 21,800 feet. The model then decelerated because of its drag to a Mach number of 0.74 at impact, which occurred 50.7 seconds after release.

#### METHODS OF CALCULATION

The data were computed in accordance with the calculation method described in reference 2. Additional computations were made to determine the additive, cowl pressure, and friction drag. The additive drag (reference 3), defined as the drag force acting parallel to the axis of symmetry on the streamlines entering the inlet, was determined by a force summation method as the difference between the momentum of the engine air flow at the inlet and the free-stream plus the axial force component on the spike of the centerbody. The axial or drag force acting on the spike was calculated from the static pressures measured along the surface of the spike. The pressure drag acting on the exterior shell was determined by the graphical integration of the static pressures acting on the cowl. The friction drag was determined from the momentum decrement obtained from the boundary-layer survey rake data. It was assumed that the effect due to static-pressure gradient along the shell was negligible at the low supersonic Mach numbers encountered in this investigation and that the static pressure and total temperature at the rake were constant through the boundary layer. The over-all friction drag was obtained by applying the coefficient based on wetted area as determined at the rake (44.36 sq ft) to the entire wetted surface of the external shell and fins (69.93 sq ft).

#### RESULTS AND DISCUSSION

The primary purpose of this investigation was to evaluate the transonic total drag and its components for a full-scale model of a 16-inch-diameter ram-jet engine operating under actual atmospheric conditions. The flight conditions encountered are shown in figure 6 wherein the Reynolds number was based on a model length of 14.3 feet. Data were observed for accelerating (rocket-on) and decelerating (rocket-off)

operation over the same free-stream Mach number range (0.8 to 1.43). At a given Mach number, rocket operation decreases the mass-flow ratio through the engine from the ratio obtained with the rocket-off condition. This change in mass-flow ratio affects the over-all drag characteristics of the ram jet. The data are therefore, in general, shown separately for the two conditions. The mass-flow ratio is defined as the ratio of engine air flow to the flow in a free-stream tube of cross-sectional area equal to the projected lip area of the cowl. The variation of mass-flow ratio  $m/m_0$  with free-stream Mach number  $M_0$  is shown in figure 7. The mass-flow ratio range covered in this investigation was from 0.66 to 0.84. Also included in figure 7 is the maximum theoretically possible mass-flow ratio which this inlet could experience through the free-stream Mach number range covered by this investigation.

In addition to the drag data, which are discussed later, it was possible to evaluate the static-pressure position error encountered by the airspeed boom and also to evaluate the total-pressure recovery across the diffuser. Figure 8 illustrates the static-pressure position error  $\Delta p$  expressed as a ratio to the free-stream dynamic pressure  $q_0$  experienced on the antenna-airspeed boom at a location 1.63 inlet diameters forward of the leading edge of the cowl. Inasmuch as the telemetered static pressure was in error by this amount through the transonic flight range, it is of interest to note the position error because, if neglected, errors could be introduced into the altitude, velocity, and Mach number when these computations are based on telemetered static pressure. However, this position error is a function of both the geometry of the inlet and the location of the static orifice and therefore is quantitatively peculiar to this particular engine. The value of  $\Delta p/q_0$  increases positively from approximately 0 at  $M_0$  of 0.8 to a maximum value at  $M_0$  of 1.04. At this point the bow wave moving downstream toward the ram jet passes over the static orifices and  $\Delta p/q_0$  drops sharply to -0.015 and then increases positively with increasing  $M_0$  and becomes approximately 0 at  $M_0 > 1.20$ . As expected, the position error is insensitive to a change in mass-flow ratio (indicated by rocket-on and rocket-off data) at  $M_0 > 1.04$  because supersonic flow exists at the orifices and the pressure disturbances generated by the ram jet cannot propagate upstream to the orifices. However, in the  $M_0$  range of 0.8 to 1.04 the flow past the orifices is subsonic and the pressure field generated by the body and augmented by the mass-flow ratio is sufficient to cause the observed errors in the static-pressure measurement.

Figure 9 shows the total-pressure recovery across the diffuser  $P_2/P_0$  and the corresponding diffuser-exit Mach number  $M_2$  as a function of  $M_0$ . The diffuser total-pressure recovery decreased from approximately 0.95 at  $M_0$  of 0.8 to 0.92 at  $M_0$  of 1.43 with sub-critical internal air flow.

### Drag Evaluations

The total drag acting on the model was defined as the sum total of the individual drags which included the cowl pressure, additive, friction, base, and internal drag.

Cowl pressure drag. - The cowl pressure drag was determined from the integration of the static-pressure distribution measured along the cowl. Figure 10 presents the cowl static pressure, expressed as a ratio to the ambient pressure  $p_c/p_0$ , as a function of  $M_0$  for the various cowl static-pressure orifices. A cross plot of these data is given in figure 11 to illustrate the axial pressure distribution along the cowl for values of constant  $M_0$ . Data are shown for the two operating conditions (rocket-on and rocket-off) to illustrate the effect on the cowl pressure distribution of a change in external air spillage resulting from a change in mass-flow ratio. For example, an increase in external air spillage (rocket-on operation) accelerated the flow over the cowl causing a decrease in the static-pressure ratio along the forward portion of the cowl ( $d/r_{max} \leq 0.4$ ) and changed the slope of the pressure ratio curve near the leading edge from negative to positive ( $d/r_{max} \leq 0.1$ ). However, at  $d/r_{max} = 1.5$  the pressure ratio is approximately 1.0 and does not vary with a change in  $M_0$  and external air spillage. The portions of the curves of figure 11 as shown by the dashed lines were arbitrarily faired to conform with the cowl shape which became conical at approximately  $d/r_{max} = 1.0$ . Figure 12 shows the corresponding pressure drag in coefficient form  $C_{Dc}$  as a function of  $M_0$ . The negative drag coefficient shown for  $M_0$  from 0.8 to 1.22 for the rocket-off condition and for  $M_0$  from 0.8 to 1.39 for the rocket-on condition indicates a net thrust acting on the cowl. As expected, a decrease in mass-flow ratio was accompanied by a decrease in the cowl pressure drag coefficient. For example, at  $M_0$  of 1.0 the cowl pressure drag coefficient changed from -0.035 to -0.062 with a decrease in mass-flow ratio (fig. 7) of 0.75 to 0.68.

Additive drag. - As a result of computing the change in momentum of the internal flow from the ram-jet outlet to the free-stream condition rather than to the ram-jet inlet, it is necessary to include the additive drag. The additive drag coefficient  $C_{Da}$  is presented in figure 13 as a function of free-stream Mach number. The maximum  $C_{Da}$  was 0.07 and occurred at  $M_0$  between 1.1 to 1.2 with the rocket on. It is obvious that a negative additive drag coefficient cannot exist under any possible flow condition at the inlet and the negative values of  $C_{Da}$  at  $M_0 \leq 0.89$  as shown by the data points are an indication of a slight error in the data in this low speed range.

In order to show more clearly the effect of mass-flow ratios and  $M_0$  on the additive drag coefficient, the data have been cross plotted in



figure 14. Additional data at higher Mach numbers are shown for a similar 16-inch-diameter ram jet which was investigated in the Lewis 8-by 6-foot supersonic tunnel (reference 4). It is readily apparent that a decrease in mass-flow ratio at constant  $M_0$  or an increase in  $M_0$  at a constant mass-flow ratio is accompanied by an increase in additive drag and is typical of subcritical engine air flow operation.

In determining the additive drag, a force summation method was used which necessitated evaluating the drag force acting on the spike of the centerbody which projected forward of the inlet. This drag expressed in coefficient form  $C_{D_s}$  was computed from the static-pressure distribution along the spike as shown by the data in figure 15. It is of interest to note the change in slope of the static-pressure ratio at the first or most forward orifice at  $M_0$  of 1.16 both with and without rocket operation. Theoretically, at supersonic  $M_0 < 1.33$  the oblique conical shock is detached and positioned as a bow wave upstream of the  $50^\circ$  cone of the central body. In figure 8 the bow wave traversed the orifices on the antenna-airspeed boom at  $M_0$  of 1.04. It is believed that at  $M_0$  of 1.16 the position and strength of the approaching bow wave are such that the interaction of the shock with the boundary layer caused boundary-layer separation, which is indicated by the decrease in static-pressure ratio at the first orifice. The theoretical static-pressure ratio for supersonic cone flow is included in figure 15. The experimental data indicate that supersonic cone flow existed at  $M_0 > 1.40$ , as shown by the static-pressure ratio of the most forward orifice which approaches the theoretical value. Since the model operates with subcritical internal flow because of the restriction in the outlet, a normal shock is also positioned ahead of the inlet at low supersonic  $M_0$ . It is believed that this shock was located between the first and second orifices, inasmuch as the static-pressure ratio for the second orifice is higher than that predicted by supersonic cone flow for the  $M_0$  range of 1.33 to 1.43. It is also noted that the boundary layer is attached, as no decrease in slope of the static-pressure ratio can be seen to indicate separation.

Friction drag. - The friction drag acting on the external surfaces of the ram jet was determined by the usual method of obtaining the momentum decrement in the boundary layer resulting from the viscous shear forces. A survey of the boundary layer was conducted by means of a total-pressure rake and a flush static orifice located 135.3 inches downstream of the leading edge of the cowl. Typical boundary-layer velocity profiles are shown in figure 16 wherein the local Mach number profile through the boundary layer is given for  $M_0$  of 0.8, 1.0, 1.2, and 1.4. Boundary-layer thickness  $\delta$  is indicated as the point at which the slope  $dy/dM_1$  increases abruptly. Data are shown for both the rocket-on and rocket-off conditions and it is apparent that the effect of the different mass flows on the Mach number profile and

boundary-layer thickness is negligible. Comparison of the boundary-layer data with the  $1/7$  power law, which was found to be most applicable to this data, is shown in figure 17. Good agreement is obtained for values of distance ratio  $y/\delta$  greater than 0.2. Below this value the experimental data deviate slightly from the empirical value, as shown.

2549 The friction drag expressed as a coefficient  $C_f$  based on wetted area is shown in figure 18. Constant Mach number curves based on experimental data are included. The theoretical curves based on von Karman equations (reference 5) for a smooth flat plate with turbulent boundary layer are included for comparison purposes. As expected, the experimental data are higher in value than the theoretical curves because of the effects of surface roughness, but it is noted that the trends of the experimental curves are similar to those of the theoretical. Figure 19 illustrates the friction drag coefficient based on maximum cross-sectional area  $C_{D_f}$  as a function of  $M_0$ . An increase in  $M_0$  is accompanied by a decrease in the friction drag coefficient. For example,  $C_{D_f}$  decreases from 0.18 to 0.13 with an increase in  $M_0$  from 0.80 to 1.43 for the rocket-on condition. The deviation of the rocket-on and rocket-off curves with decreasing  $M_0$  is attributed to the corresponding divergence in Reynolds numbers between the two conditions.

Base drag. - The base drag resulting from the lower than atmospheric pressures occurring on the flat base of the annular restriction is shown in figure 20; also included are the base static-pressure ratio and the static-pressure ratio of the exhaust jet issuing from the center of the annular base. The data are shown for both the rocket-on and rocket-off conditions. In general, an increase in  $M_0$  was accompanied by a decrease in base pressure ratio despite a large increase in jet static-pressure ratio. In the transonic Mach number range, an abrupt drop in base pressure ratio occurred at  $M_0$  of 0.97 for both the rocket-on and rocket-off operating conditions, followed by a partial recovery in the base pressure ratio at  $M_0$  of 1.16 for the rocket-off condition and at  $M_0$  of 1.32 for the rocket-on condition. This transonic base pressure drop is not attributed to the jet pressure ratio as no abrupt change in this data can be seen. It is believed to be largely a transonic phenomenon associated with the free-stream conditions. However, the delayed recovery for the rocket-on condition ( $M_0 = 1.32$ ) as compared with the rocket-off condition ( $M_0 = 1.16$ ) suggests a possible aspirating effect caused by the higher jet exhaust velocities associated with the rocket-on condition. It is also possible that this partial base pressure recovery may be an unstable flow phenomenon and that the apparent hysteresis loop in the data may be due to the direction (accelerating or decelerating) with which the test condition was approached. A general comparison is made with the base data obtained from solid bodies of revolution (reference 6) and from blunt trailing-edge airfoil sections (reference 7). As can be seen from figure 20, the annular base

data in the subsonic  $M_0$  range are approximately halfway between the body of revolution and airfoil data. However, above  $M_0$  of 1.10 the annular data agree closely with the airfoil base data. These data are lower than the body of revolution data, indicating that higher base drags were encountered. The base drag coefficient  $C_{D_b}$  clearly illustrates the drag penalty incurred by this transonic decrease in base static pressure. For the rocket-off condition,  $C_{D_b}$  increased from a subsonic value of 0.23 to an average maximum of 0.35 in an  $M_0$  range of 1.02 to 1.15 followed by a gradual decrease to a  $C_{D_b}$  of 0.25 at  $M_0$  of 1.30. For the rocket-on condition, the maximum  $C_{D_b}$  was 0.33.

Internal drag. - The internal drag was determined from the change in momentum of the internal engine air flow from the free-stream conditions to the engine outlet. The data are presented in coefficient form in figure 21 for both the rocket-on and rocket-off conditions. The rocket-on data are based only on the loss in momentum of the intake air and do not include the momentum of the rocket exhaust gas. The internal drag coefficient  $C_{D_i}$  remained approximately constant at 0.04 for the rocket-on condition for free-stream Mach numbers from 0.80 to 1.43. As expected, the rocket-off condition, which had higher mass flows at a given  $M_0$  than the rocket-on condition, had a corresponding higher  $C_{D_i}$ . For example, at  $M_0$  of 1.00,  $C_{D_i}$  increased from 0.04 to 0.06.

In order to compare the summation of the drag forces with the direct measurement obtained from the accelerometer data, it is necessary to include the thrust coefficient of the rocket based on ram-jet cross-sectional area for the rocket-on condition. The variation of the rocket thrust coefficient with  $M_0$  is shown in figure 22. This curve was calculated from the rocket performance data given in reference 8.

Total drag. - The total drag coefficient is shown in figure 23 as a function of  $M_0$  for the rocket-off condition. The total drag coefficient curve is the summation of the individual drag coefficients which were based on pressure measurements, as previously discussed. In figure 23 this curve is compared with the total drag coefficient data points obtained independently from the accelerometer data. The agreement between the two methods of obtaining the total drag coefficient is very good with a maximum deviation of only 6 percent of the over-all value. Part of this discrepancy may be due to interference drag between the four stabilizing fins and the body, as no allowance for interference drag was made in the summation method of obtaining the total drag coefficient curve. Figure 23 also illustrates the magnitude of the individual drag forces relative to each other and to the total drag. It is noted that the addition of the base drag coefficient to the external drag coefficient more than doubles the value of the external drag coefficient. At  $M_0$  of 1.15, the base drag amounted to 57 percent of

2549 the total drag. The external drag coefficient, excluding base drag, had a minimum value of 0.13 at  $M_0$  of 0.90 and then gradually increased with no abrupt change in the transonic range to a maximum value of 0.20 at  $M_0$  of 1.30 followed by a gradual decrease to 0.17 at  $M_0$  of 1.43. Over the range of this investigation, the external drag is predominantly a result of the friction drag. It is also apparent from figure 23 that the abrupt increase in total drag coefficient in the transonic  $M_0$  range of 0.97 to 1.15 was largely due to the increase in the base drag coefficient. Also of interest is the fact that at  $M_0 < 1.0$  for the mass-flow ratio encountered with the rocket-off condition the values of  $C_{D_e}$  plus  $C_{D_c}$  are negative, indicating a net thrust effect on the engine as opposed to the conventional assumption that subsonically the sum of additive and cowl pressure drag approximates zero. However, for the range of mass flows encountered with the rocket-on condition, the sum of additive and cowl pressure drag was approximately zero, as shown in figure 24. Therefore, it may be that the validity of this assumption is dependent on the mass-flow ratio as shown and possibly on the geometry of the inlet.

The drag data for the rocket-on condition are presented in figure 24. However, since the accelerometer measured the acceleration resulting from the net force (thrust minus drag) acting on the model, the propulsive thrust coefficient could be computed directly. For comparison with the summation of the individual drags it was necessary to subtract the total drag coefficient from the rocket thrust coefficient (fig. 22) in order to obtain a propulsive thrust coefficient curve as shown in figure 24. It is apparent that good agreement was obtained between the data points and the curve, indicating that satisfactory accuracy was realized during the accelerating, rocket-on phase of the flight. The external drag coefficient had a minimum value of 0.17 at  $M_0$  of 0.93, which was approximately 30 percent higher than the minimum value obtained with the rocket-off condition. This increase was due to the increase in additive drag coefficient resulting from the change in mass-flow ratio in this  $M_0$  range from the rocket-off to the rocket-on condition. The external drag coefficient increased gradually from 0.17 to a maximum value of 0.21 at  $M_0$  of 1.25 and then decreased to 0.18 at  $M_0$  of 1.43.

#### Drag Comparison

Figure 25 presents a comparison of the measured drag coefficient and the base static-pressure ratio of this model with the results (reference 2) obtained from three other models previously investigated. Data are shown only for the rocket-off condition as the internal drag coefficient was not available for all the models during the rocket-on

~~CONFIDENTIAL~~

~~CONFIDENTIAL~~

operation. The four models were similar except for the size of the annular restriction. Included in figure 25 are the inside diameters of the restrictions and the areas of the annular flat bases. Inasmuch as there is only a very limited amount of transonic experimental data available for annular flat bases with flow issuing from their centers, the base static-pressure ratios were included for all the models. Close agreement of the annular base data among the four models investigated is observed; apparently the effect of base area on the base static-pressure ratio is small for the range of base areas investigated.

The four models were not precisely identical because of slight variations in surface roughness and fabrication procedure, and therefore only a general comparison should be made. The reduction in mass flow caused a decrease in internal drag to occur with a decrease in outlet diameter at a given  $M_0$ . However, as expected, the base drag was increased with an increase in base area. For example, at  $M_0$  of 1.10 the internal drag coefficient decreased from 0.11 to 0.02 and the base drag coefficient increased from 0.31 to 0.41 with an increase in base area obtained by comparing the data from model 3 with the data from model 1. At  $M_0$  of 0.90 model 3 had the highest total drag coefficient of 0.50 due to the fact that it had the highest internal drag coefficient, which at this  $M_0$  apparently outweighed the relative effects of the other drags. The maximum total drag coefficient was 0.63 at  $M_0$  of 1.16 and occurred with model 1, which had the largest annular base area.

#### SUMMARY OF RESULTS

As part of a free-flight transonic drag investigation on full-scale models of a 16-inch-diameter ram-jet engine, one model was instrumented sufficiently that the constituents of the total drag could be evaluated. The model was dropped from an airplane at 35,000 feet of altitude, rocket-propelled to a Mach number of 1.43, and then decelerated through the transonic range before impact. Data were obtained over the same Mach number range for rocket-on and rocket-off operation. The following results were obtained:

1. It was possible to account for at least 94 percent of the total drag as determined directly from accelerometer data by a summation of the constituent drags, that is, cowl pressure, additive, friction, base, and internal drag, each of which was determined independently from pressure measurements.

2. Negative cowl pressure drag coefficients were obtained at Mach numbers less than 1.22 and 1.39 for the rocket-off and rocket-on conditions, respectively, indicating a net thrust acting on the cowl.

~~CONFIDENTIAL~~

3. Good agreement was obtained between the experimental boundary-layer velocity profiles and those predicted by the  $1/7$  power law at radial distances greater than 20 percent of the boundary-layer thickness from the body. Below this value the experimental data deviated slightly from the empirical predicted values.

4. The average maximum base drag coefficient of 0.35 occurred over a Mach number range of 1.02 to 1.15 for the rocket-off condition as compared with 0.32 over a greater Mach number range of 1.02 to 1.32 for the rocket-on condition. At  $M_0$  of 1.15 (rocket-off condition), the base drag amounted to 57 percent of the total drag.

5. The external drag coefficient, excluding base drag, for the rocket-off condition had a minimum value of 0.13 at a Mach number of 0.90 and gradually increased with no abrupt change in the transonic range to a maximum value of 0.20 at 1.30

6. The conventional subsonic assumption for a ducted body which discharges to ambient pressure is that the sum of the additive and cowl pressure drag coefficient is approximately zero. Data have been presented which indicate that this may not be a valid assumption and is influenced by the mass-flow ratio.

Lewis Flight Propulsion Laboratory  
National Advisory Committee for Aeronautics  
Cleveland, Ohio

## REFERENCES

1. Rabb, Leonard, and North, Warren J.: Free-Flight Performance of 16-Inch-Diameter Supersonic Ram-Jet Units. IV - Performance of Ram-Jet Units Designed for Combustion-Chamber-Inlet Mach Number of 0.21 at Free-Stream Mach Number of 1.6 Over a Range of Flight Conditions. NACA RM E50L18, 1951.
2. Messing, W. E., and Acker, Loren W.: Transonic Free-Flight Drag Results of Full-Scale Models of 16-Inch-Diameter Ram-Jet Engines. NACA RM E52B19, 1952.
3. Ferri, Antonio, and Nucci, Louis M.: Preliminary Investigation of a New Type of Supersonic Inlet. NACA TN 2286, 1951.
4. Nussdorfer, T., Wilcox, F., and Perchonok, E.: Investigation at Zero Angle of Attack of a 16-Inch Ram-Jet Engine in 8- by 6-Foot Supersonic Wind Tunnel. NACA RM E50L04, 1951.
5. de Kármán, Th.: The Problem of Resistance in Compressible Fluids. Quinto Convegno "Volta", Reale Accademia d'Italia (Roma), Sett. 30 - Ott. 6, 1935, pp. 3-57.
6. Faro, I. D. V.: Experimental Determination of Base Pressures at Supersonic Velocities. Bumblebee Rep. No. 106, Johns Hopkins Univ., Appl. Phys. Lab., Nov. 1949. (Contract NOrd 7386, Bur. of Ordnance, U. S. Navy.)
7. Morrow, J. D., and Katz, Ellis: Flight Investigation at Mach Numbers from 0.6 to 1.7 to Determine Drag and Base Pressures on a Blunt-Trailing-Edge Airfoil and Drag of Diamond and Circular-Arc Airfoils at Zero Lift. NACA RM L50E19a, 1950.
8. Anon.: Jato Manual SPIA/MI. Solid Propellant Information Agency, Appl. Phys. Lab., Johns Hopkins Univ., March 1949.

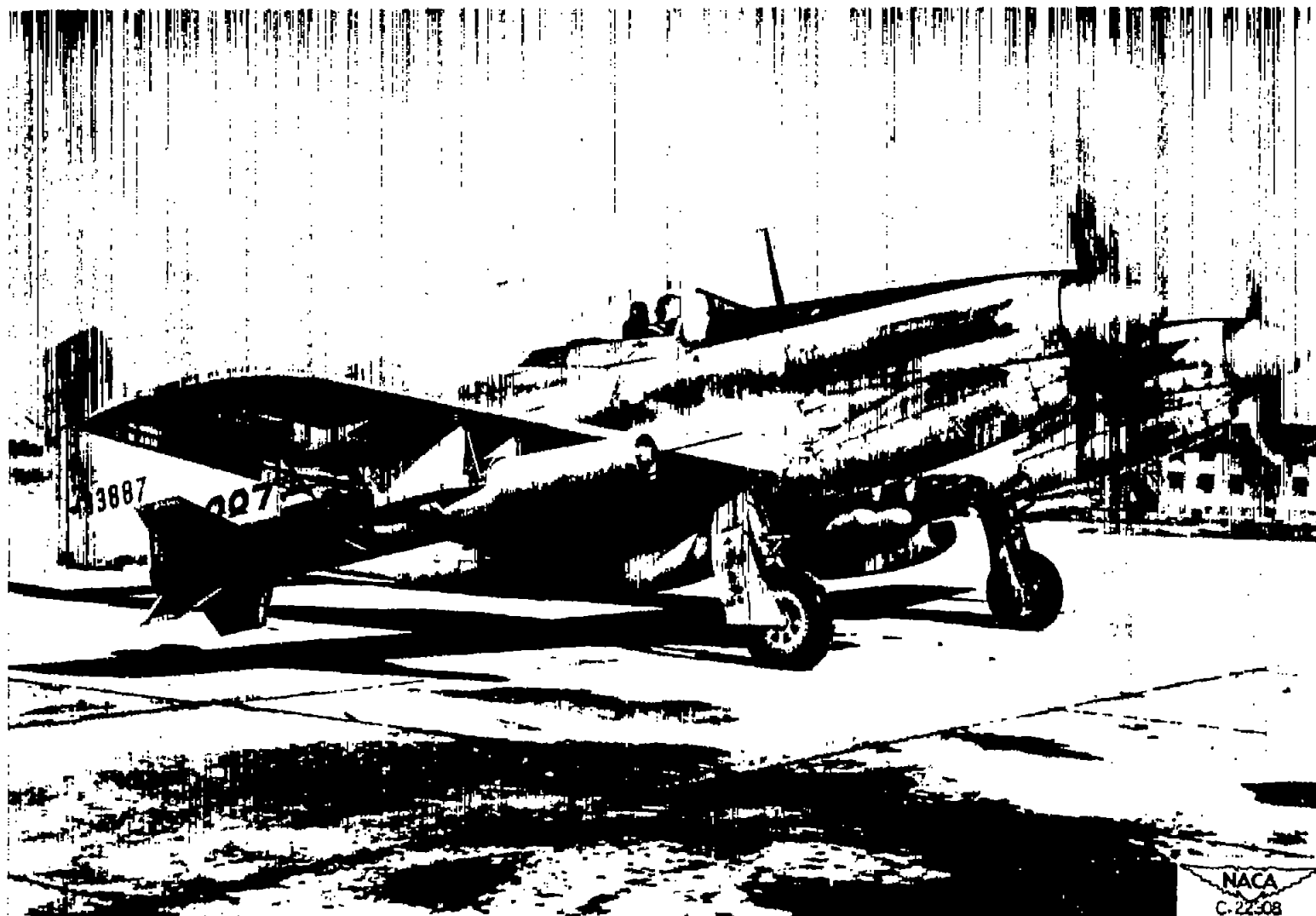
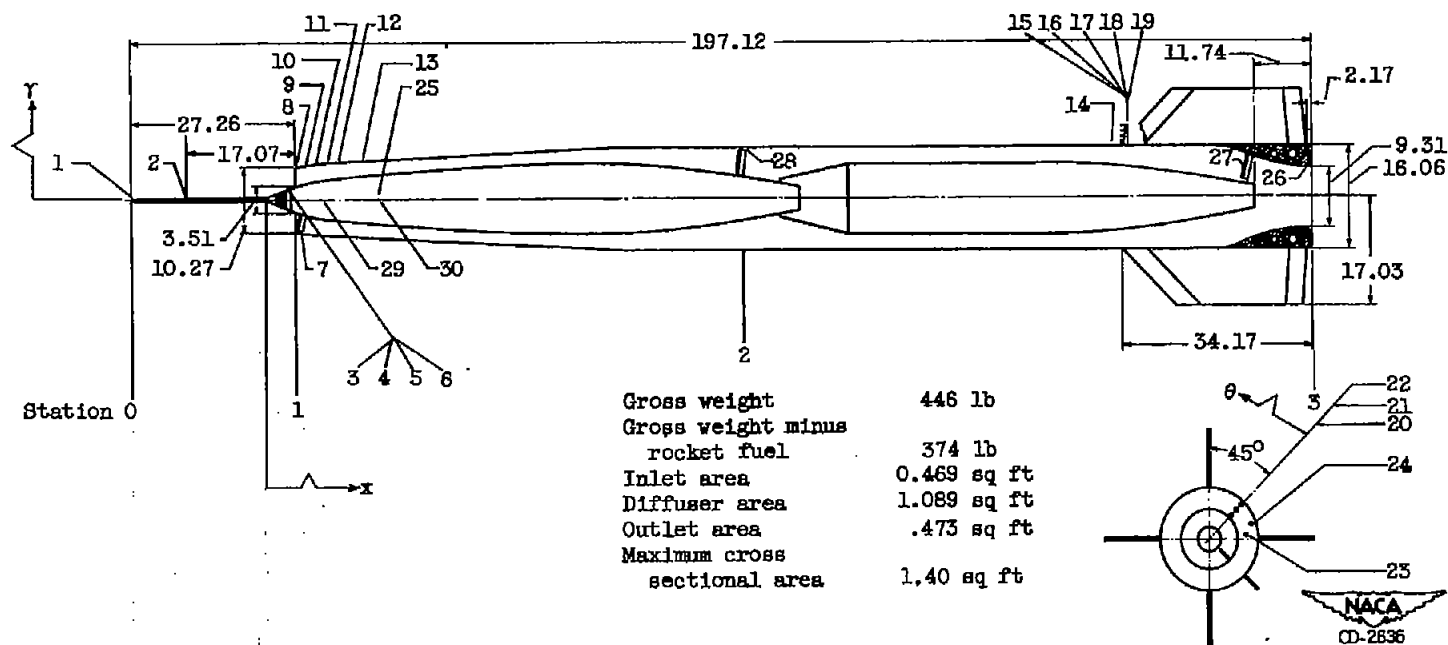


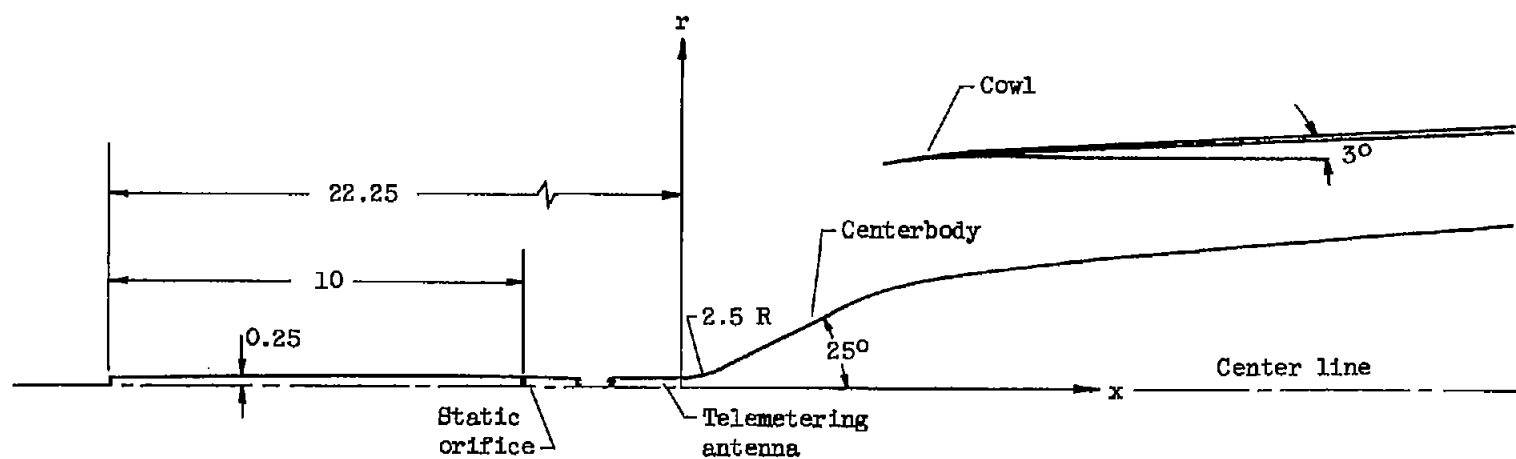
Figure 1. - Photograph of drag model of 18-C-type ram-jet engine mounted beneath right wing of F-82 airplane.





Instrument	Measurement	Location			Instrument	Measurement	Location			Instrument	Measurement	Location		
		x (in.)	r (in.)	$\theta$ (deg)			x (in.)	r (in.)	$\theta$ (deg)			x (in.)	r (in.)	$\theta$ (deg)
1	$P_0$	-22.38	----	--	11	$P_c$	6.27	5.46	99	21	$P_b$	174.74	6.313	0
2	$P_0$	-12.19	----	--	12	$P_c$	7.25	5.56	102	22	$P_b$	174.74	7.563	0
3	$P_s$	1.11	0.57	--	13	$P_c$	16.88	6.00	105	23	$P_b$	174.74	6.188	316
4	$P_s$	3.43	1.75	--	14	$P_f$	140.16	8.03	267	24	$P_b$	174.74	7.438	328
5	$P_s$	4.40	2.25	--	15	$P_f$	140.57	8.156	270	25	$a_n$	27.0	-----	-----
6	$P_l$	5.46	2.70	--	16	$P_f$	140.57	8.563	270	26	$P_3$	174.46	4.656	316
7	$P_l$	5.44	2.70	--	17	$P_f$	140.57	9.313	270	27	$P_3$	162.99	6.047	270
8	$P_c$	5.06	5.20	90	18	$P_f$	140.57	10.047	270	28	$P_2$	79.125	3.687	90
9	$P_c$	5.32	5.26	93	19	$P_f$	140.57	11.031	270	29	$a_n$	14.25	-----	-----
10	$P_c$	5.69	5.35	96	20	$P_b$	174.74	5.063	0	30	$a_n$	27.00	-----	-----

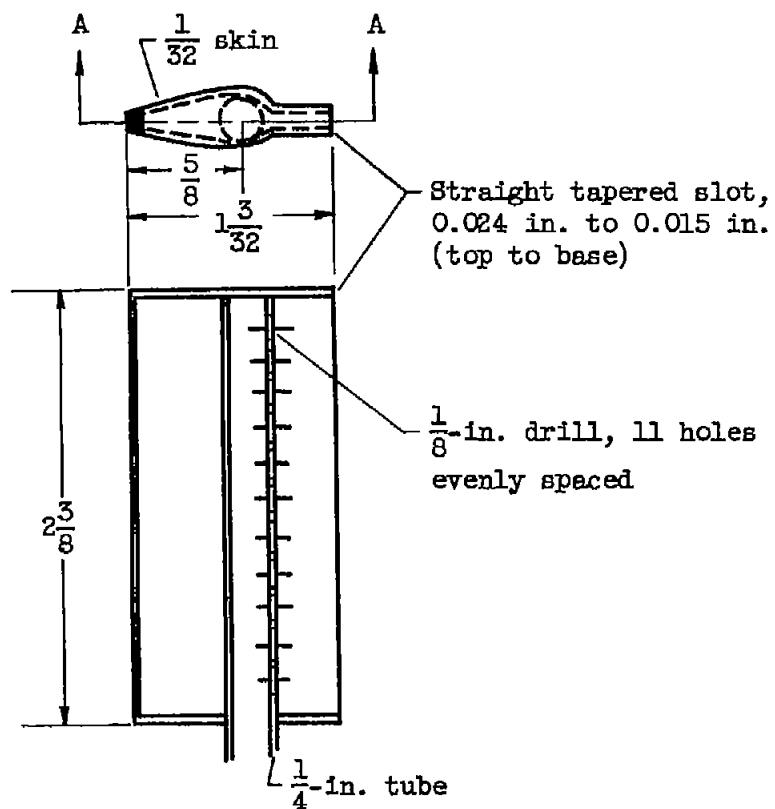
Figure 2. - Schematic diagram of drag model of 16-inch-diameter ram-jet engine including location of instrumentation pickups. (All dimensions are in inches.)



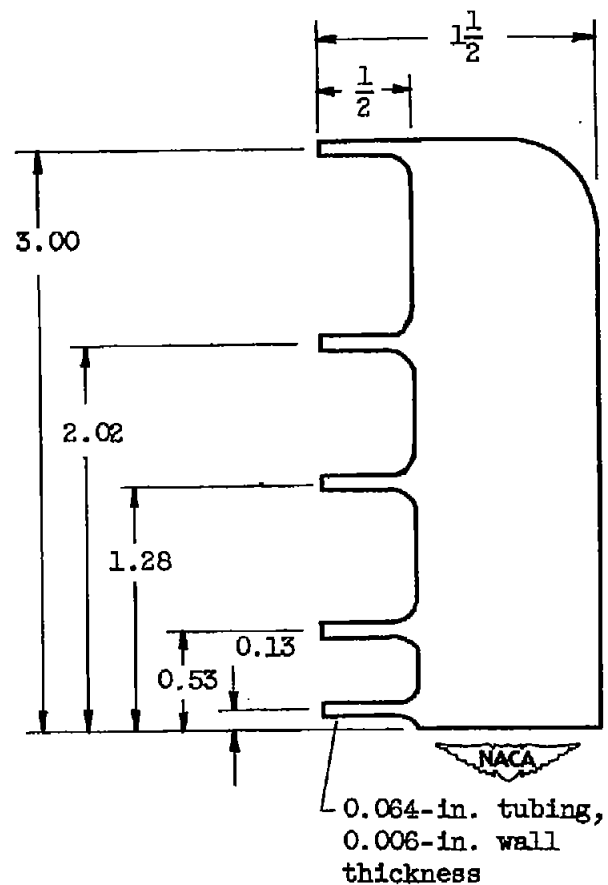
External spike coordinates		External cowl coordinates	
Station, x	Ordinate, r	Station, x	Ordinate, r
0	0.250	4.821	5.234
3.77	1.758	5.071	5.285
4.17	1.930	5.571	5.361
4.57	2.090	6.071	5.424
4.97	2.232	6.571	5.469
5.37	2.340	3° taper to cylinder at station 53.50	
5.77	2.425		
6.17	2.503		
6.57	2.573		



Figure 3. - Schematic diagram of inlet of 16-inch-diameter ram-jet engine including design specifications.  
(All dimensions are in inches.)

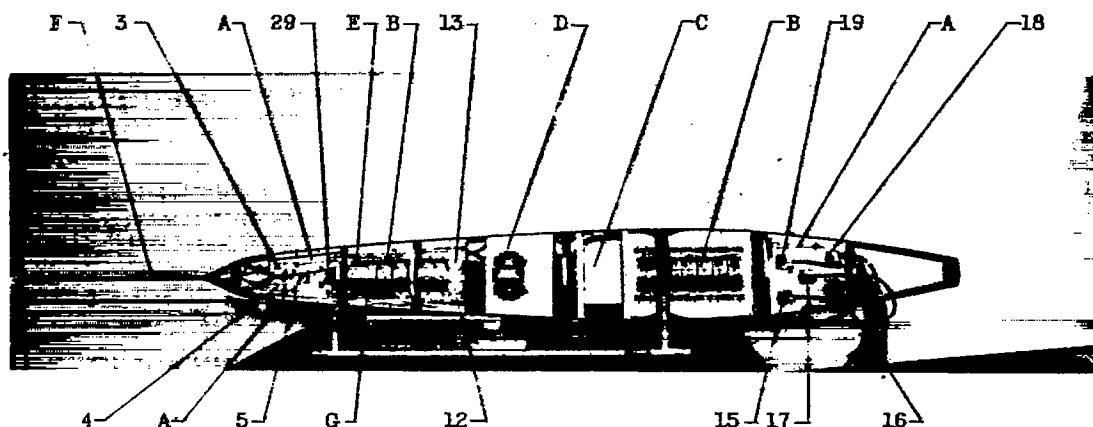



Self-averaging total-  
head probe



Boundary-layer total-head survey rake

Figure 4. - Schematic sketch of self-averaging total-head probe and boundary-layer total-head survey rake for 16-inch-diameter ram-jet engine. (All dimensions are in inches.)

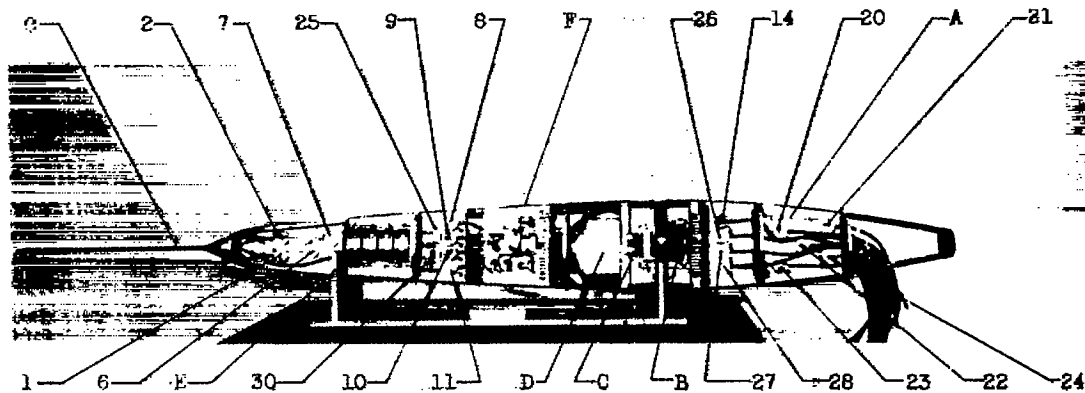


Instru- ment	Transducer		Frequency (kc)
	Pressure	Range (lb/sq in. abs)	
3	Cone, 1	3 - 15	150
4	Cone, 2	3 - 15	190.5
5	Cone, 3	3 - 15	150
12	Cowl, 5	1 - 15	170
13	Cowl, 6	1 - 15	170
15	Friction total, 1	3 - 26	129.5
16	Friction total, 2	3 - 26	129.5
17	Friction total, 3	3 - 26	129.5
18	Friction total, 4	3 - 26	110
19	Friction total, 5	3 - 26	110
	Acceleration	(ft/sec <sup>2</sup> )	
29	Accelerometer, 1	0 to -128.5	199.5
	Letter	Designation	 C-28291
	A	Heater	
	B	Oscillators	
	C	Insulated battery compartment	
	D	Dynamotor	
	E	Transmitter	
	F	Antenna-airspeed boom	
	G	Modulator	

NACA  
C-28291

(a) Top view.

Figure 5. - Telemeter instrumentation for drag model of 16-inch-diameter ram-jet configuration with 10-channel telemetering system and 30 commutable oscillators.



Instrument	Transducer	Range	Frequency (kc)
	Pressure	(lb/sq in. abs)	
1	Free-stream total	3 - 26	179.5
2	Free-stream static	3 - 15	160.5
6	Inlet static	2 - 18	199.5
7	Inlet total	3 - 28	190.5
8	Cowl static, 1	1 - 15	129.5
9	Cowl static, 2	1 - 15	160.5
10	Cowl static, 3	1 - 15	110
11	Cowl static, 4	1 - 15	170
14	Free-stream shell static	3 - 15	110
20	Base static, 1	2 - 14	119.5
21	Base static, 2	2 - 14	119.5
22	Base static, 3	2 - 14	119.5
23	Base static, 4	2 - 14	119.5
24	Base static, 5	2 - 14	179.5
26	Exit static	3 - 15	150
27	Exit total	3 - 26	179.5
28	Free-stream total minus diffuser total	0 - 10	160.5
	Acceleration	(ft/sec <sup>2</sup> )	
30	Accelerometer, 2	160 to -160	139.5
25	Accelerometer, 3	0 to -80	139.5
Letter	Designation	Letter	Designation
A	Heater	E	Oscillators
B	Switching assembly	F	Power supply panel
C	Motor drive for switching assembly	G	Antenna boom static
D	Insulated battery compartment		

(b) Bottom view.

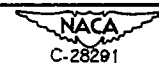


Figure 5. - Concluded. Telemeter instrumentation for drag model of 16-inch-diameter ram-jet configuration with 10-channel telemetering system and 30 commutable oscillators.

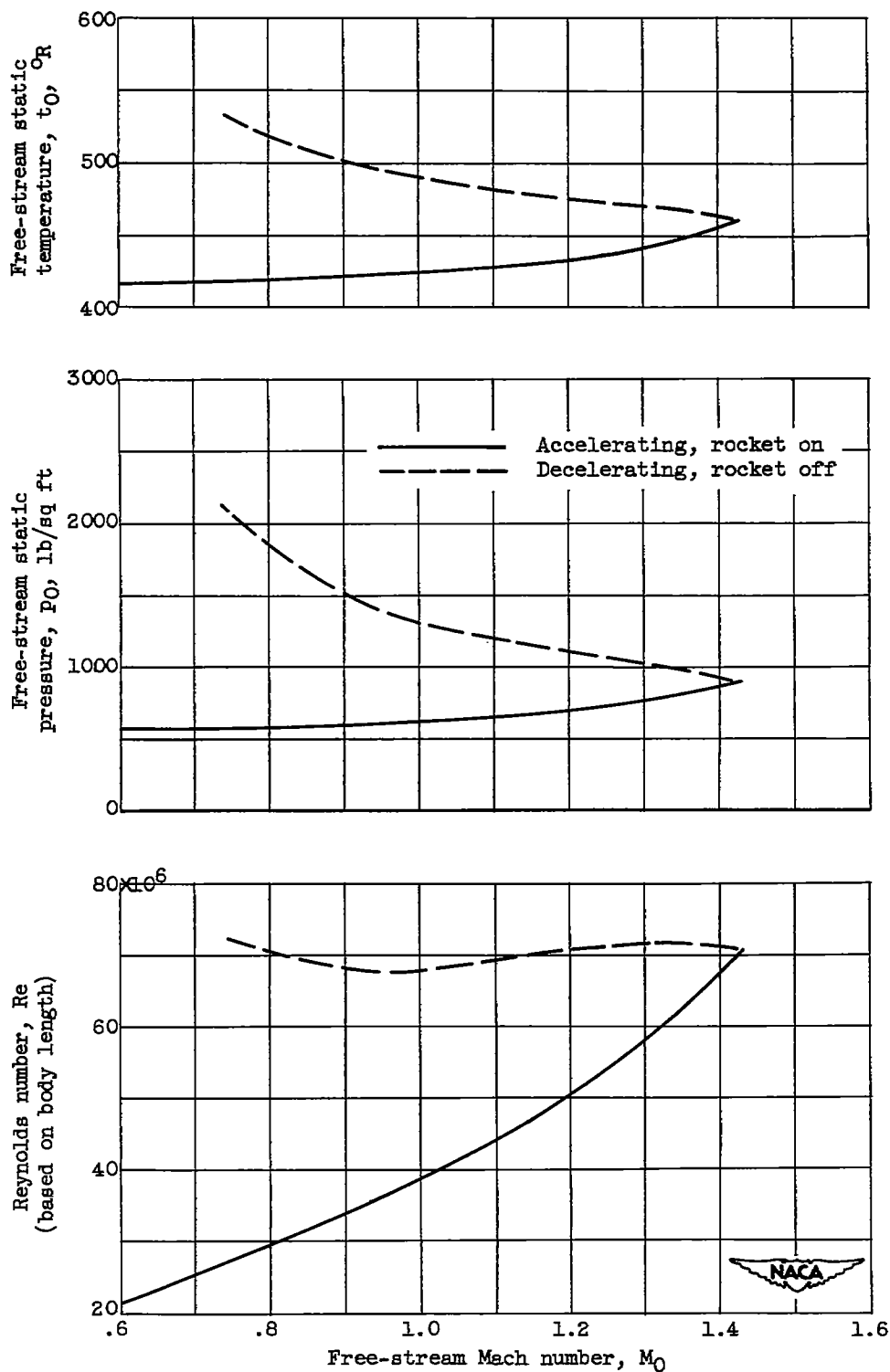


Figure 6. - Free-stream flight conditions as function of free-stream Mach number.

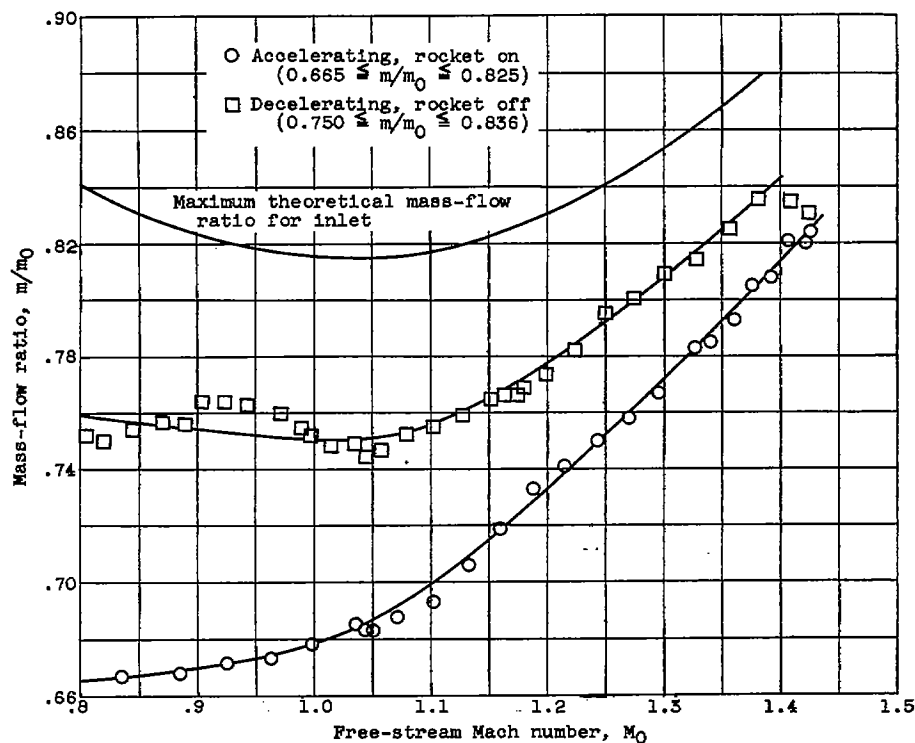


Figure 7. - Effect of free-stream Mach number on mass-flow ratio for rocket-on and rocket-off conditions.

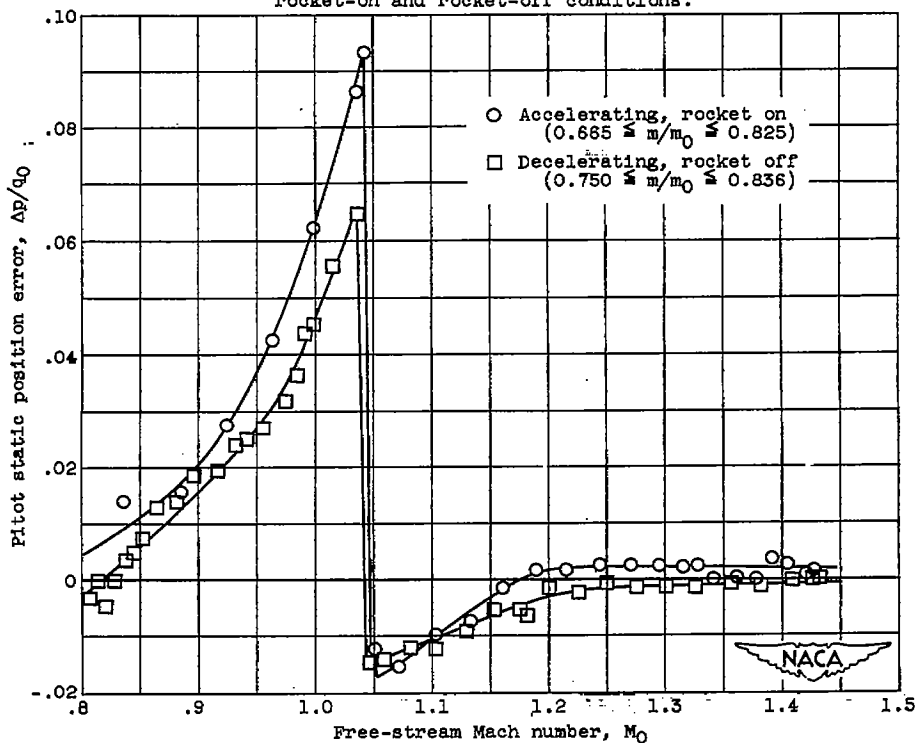


Figure 8. - Effect of free-stream Mach number on pitot static position error for rocket-on and rocket-off conditions.

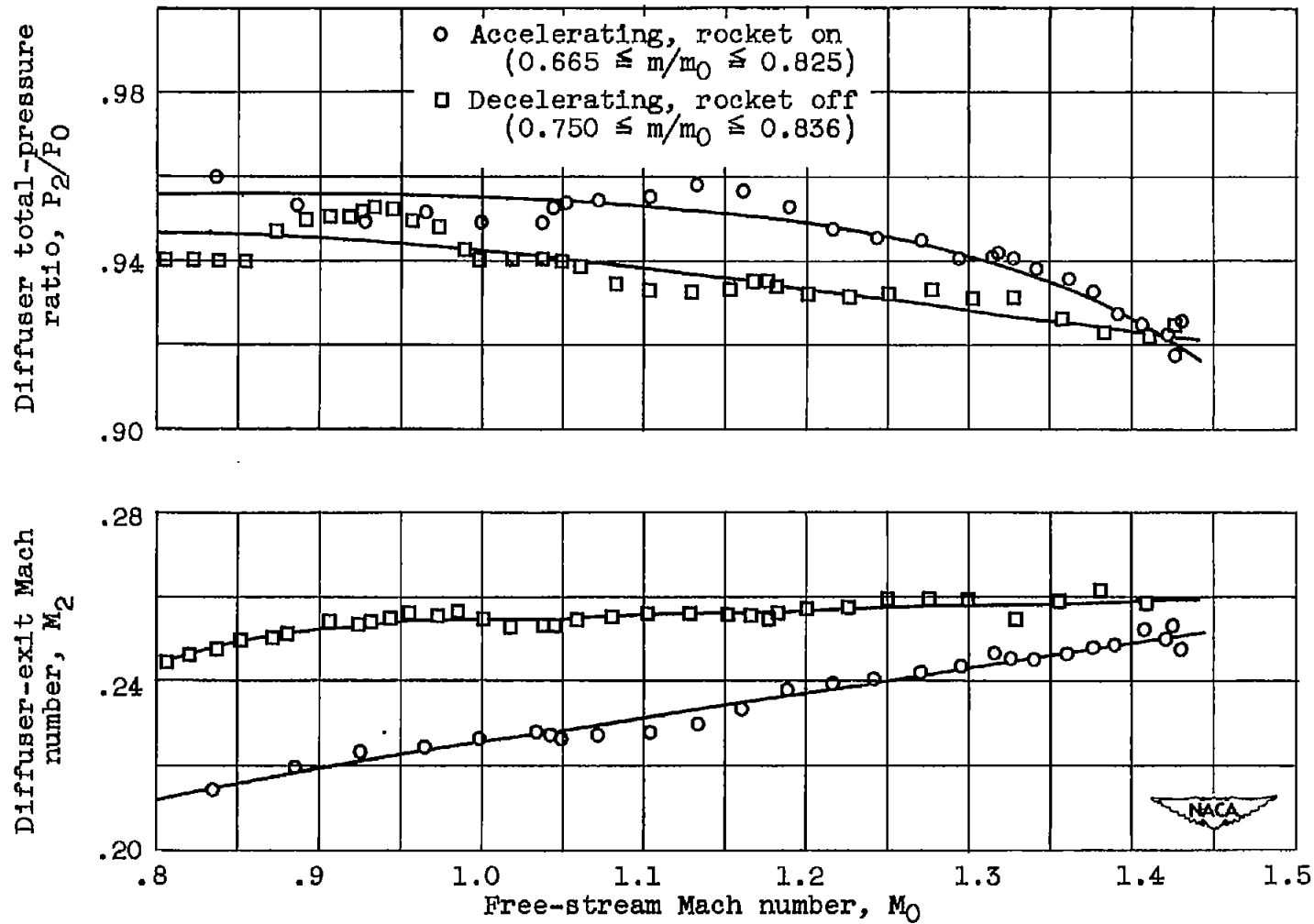


Figure 9. - Effect of free-stream Mach number on diffuser-exit Mach number and diffuser total-pressure ratio for rocket-on and rocket-off conditions.



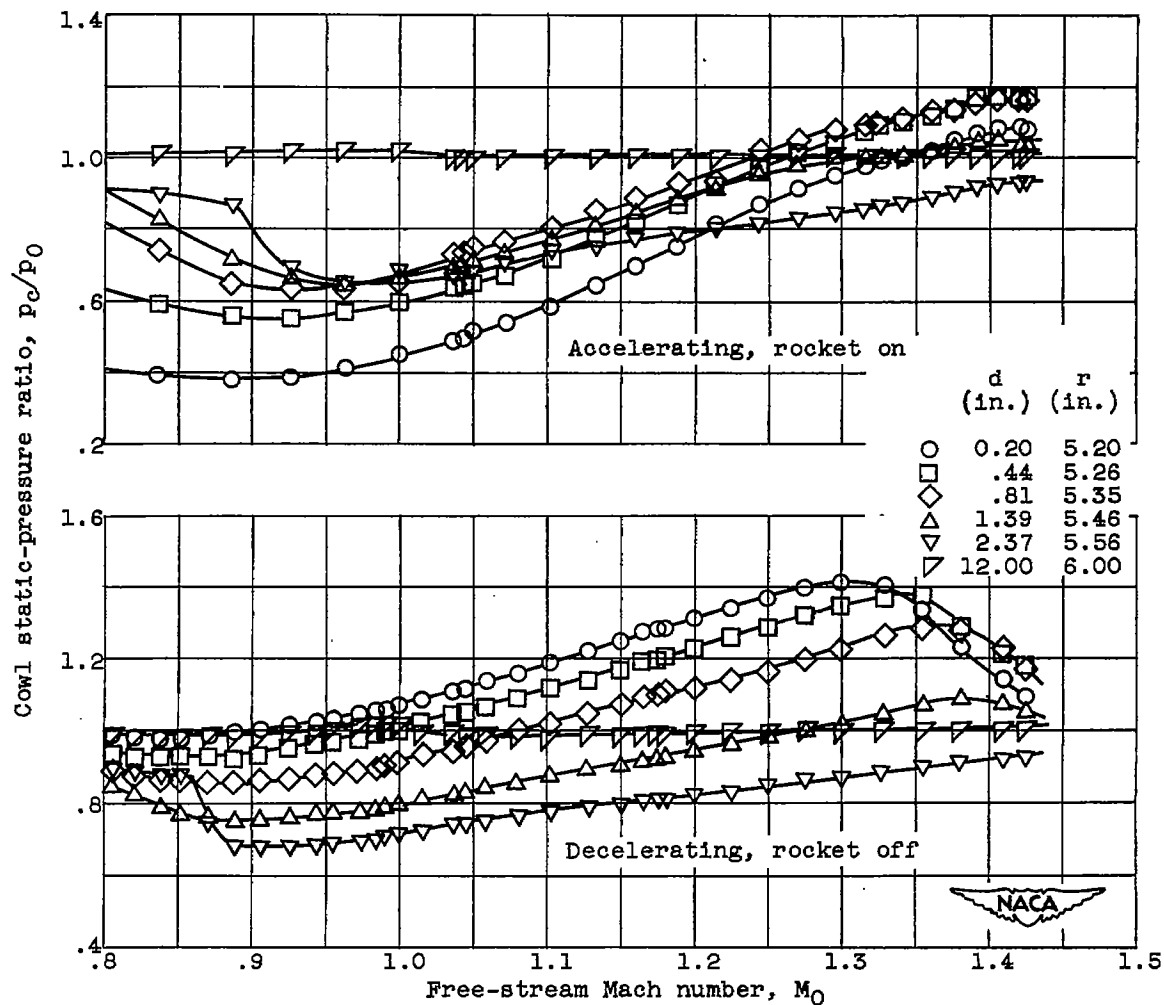
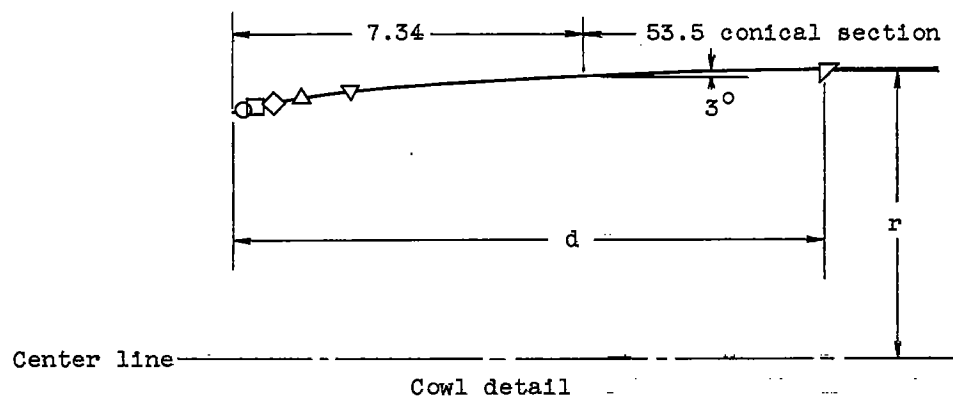


Figure 10. - Effect of free-stream Mach number on cowl static-pressure ratio for rocket-on and rocket-off conditions.

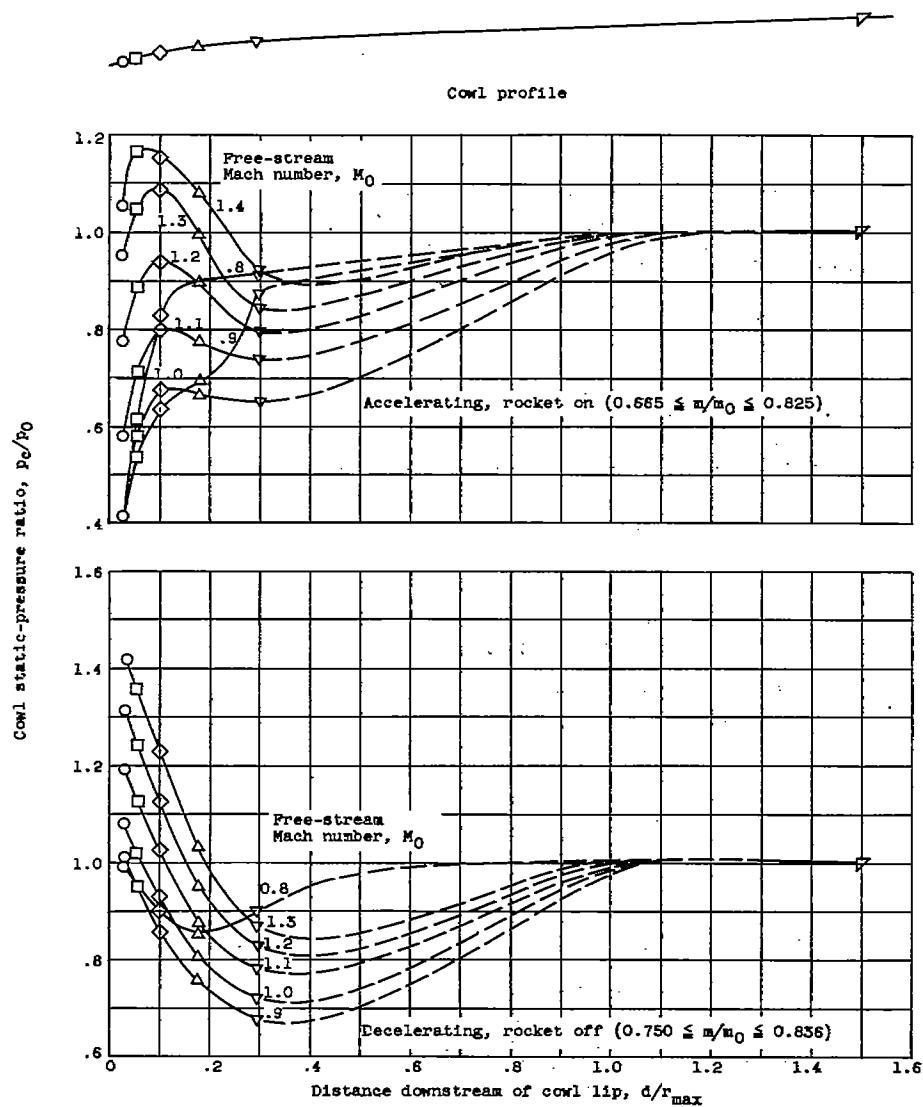


Figure 11. - Cowl static-pressure ratio as function of distance ratio for constant free-stream Mach numbers.

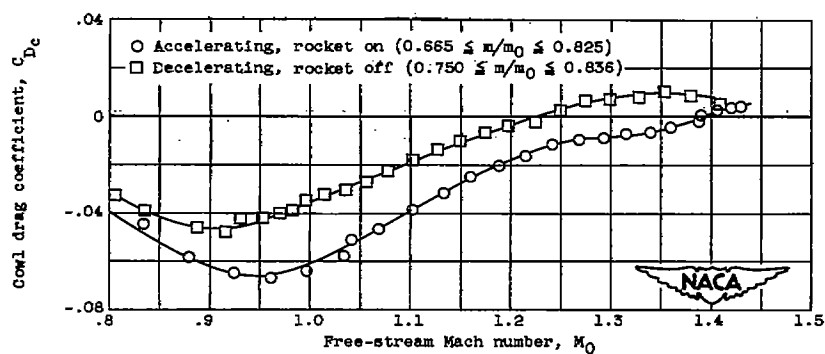


Figure 12. - Effect of free-stream Mach number on cowl drag coefficient for rocket-on and rocket-off conditions.

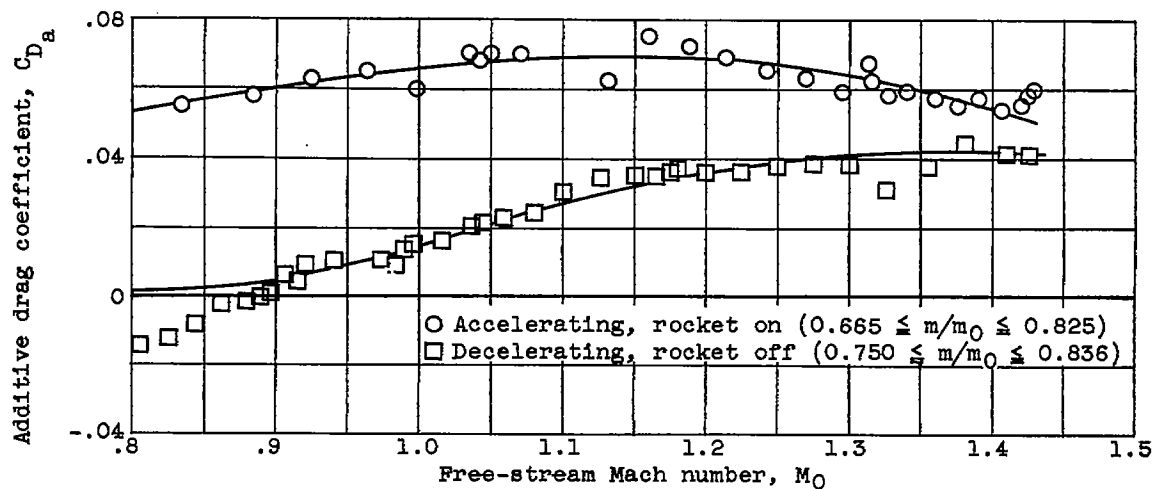


Figure 13. - Effect of free-stream Mach number on additive drag coefficient for rocket-on and rocket-off conditions.

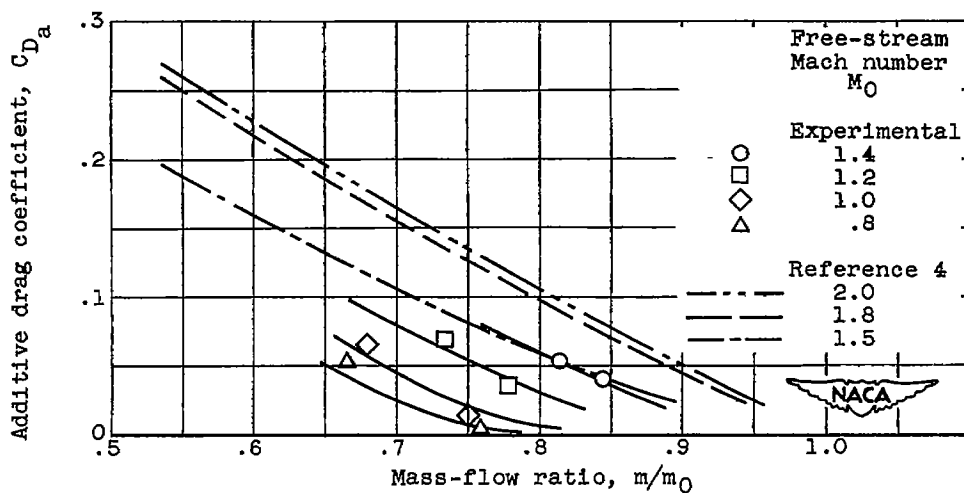


Figure 14. - Effect of free-stream Mach number and mass-flow ratio on additive drag coefficient.

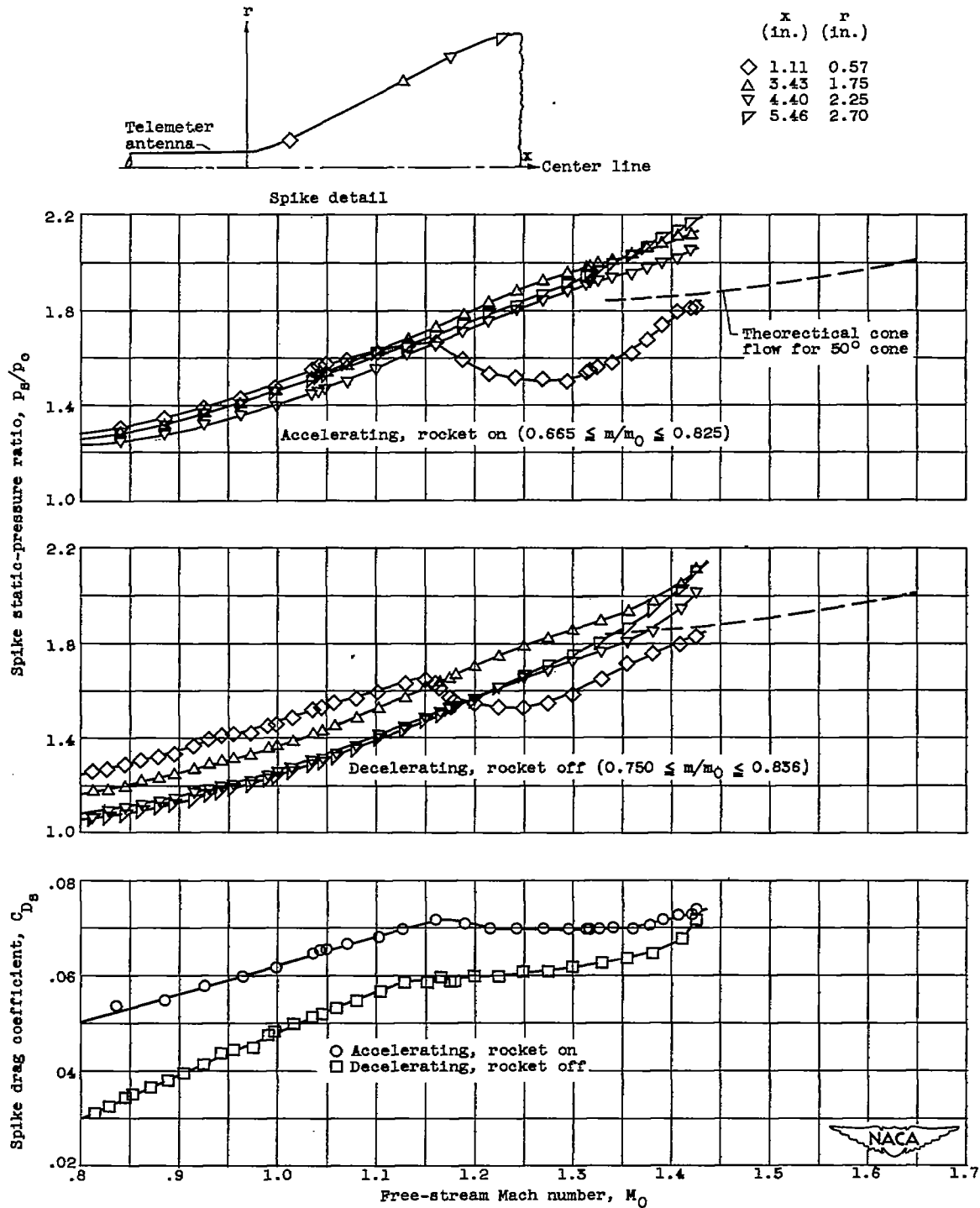


Figure 15. - Effect of free-stream Mach number on spike static-pressure ratio and drag coefficient for rocket-on and rocket-off conditions.

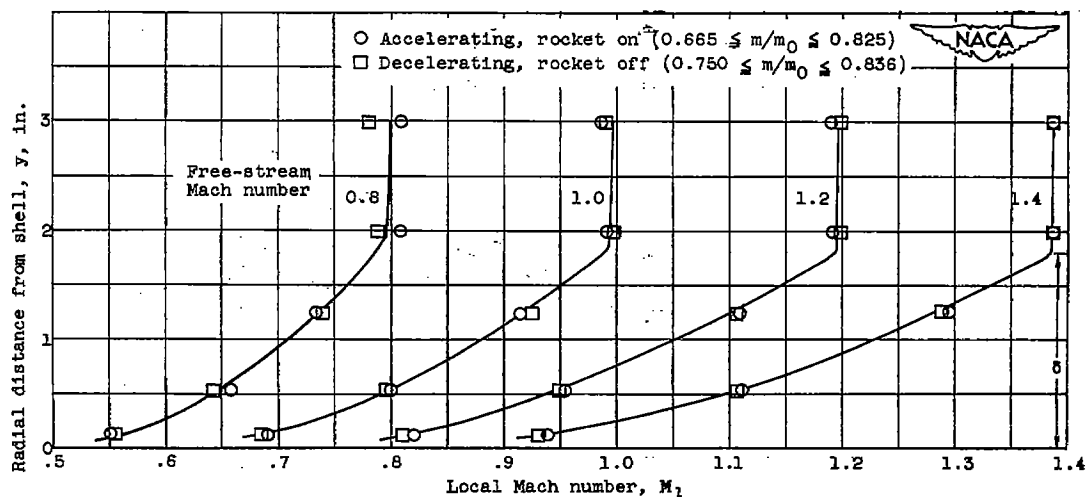


Figure 16. - Variation in local Mach number through boundary layer for free-stream Mach numbers of 0.8, 1.0, 1.2, and 1.4.

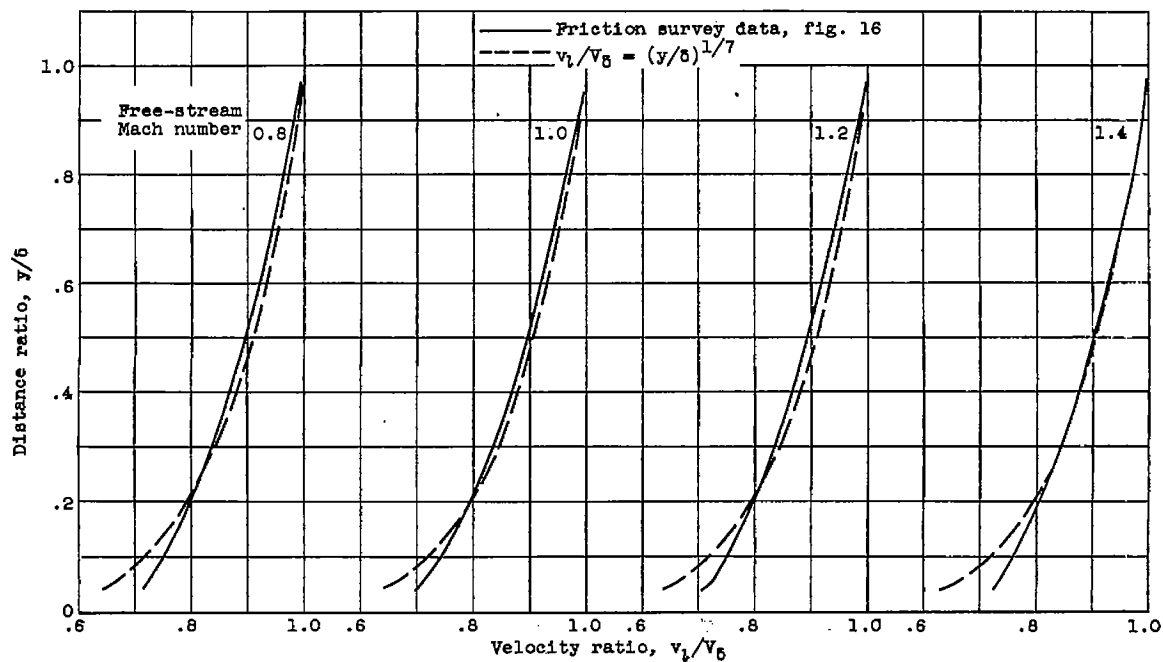


Figure 17. - Boundary-layer velocity profile for free-stream Mach numbers of 0.80, 1.0, 1.2, and 1.4.

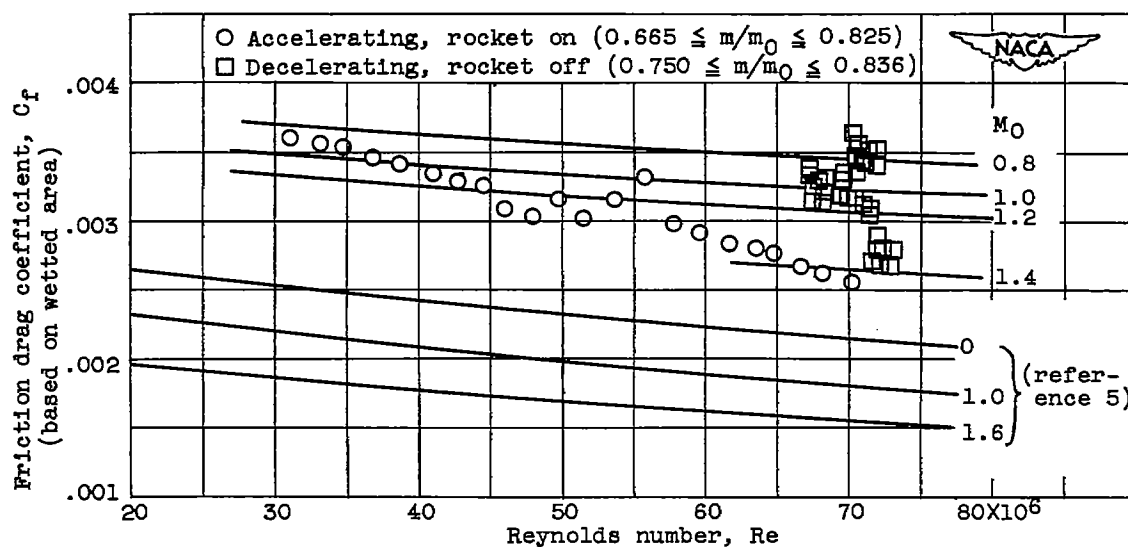


Figure 18. - Effect of Reynolds number on friction drag coefficient based on wetted area.

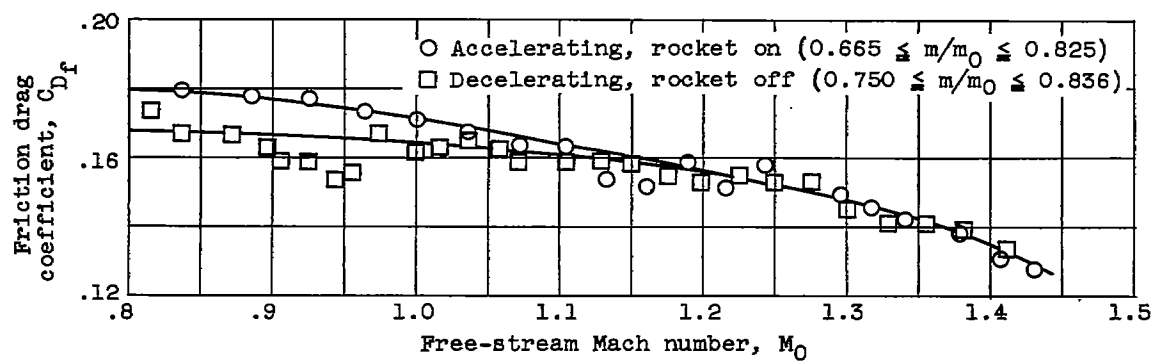


Figure 19. - Friction drag coefficient as function of free-stream Mach number for rocket-on and rocket-off conditions.

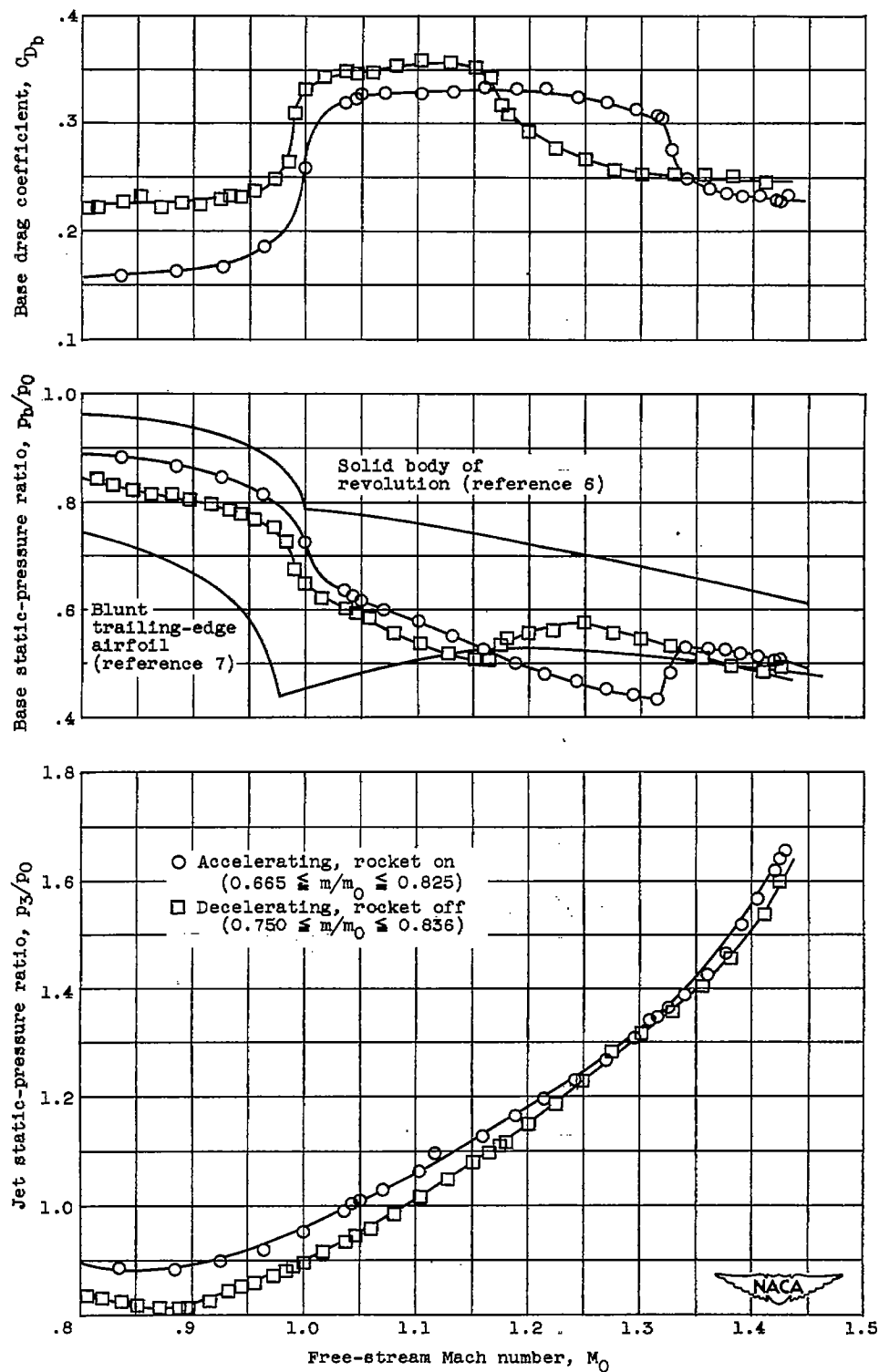


Figure 20. - Effect of free-stream Mach number on base and jet static-pressure ratio and base drag coefficient for rocket-on and rocket-off conditions.

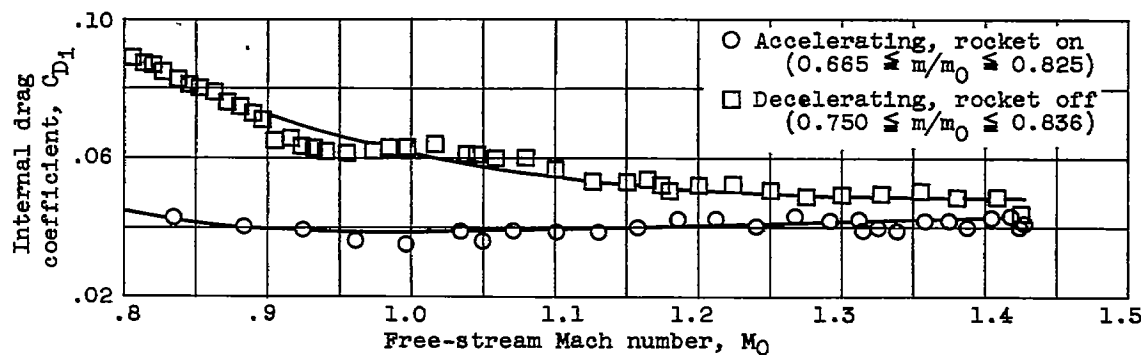


Figure 21. - Effect of free-stream Mach number on internal drag coefficient for rocket-on and rocket-off conditions.

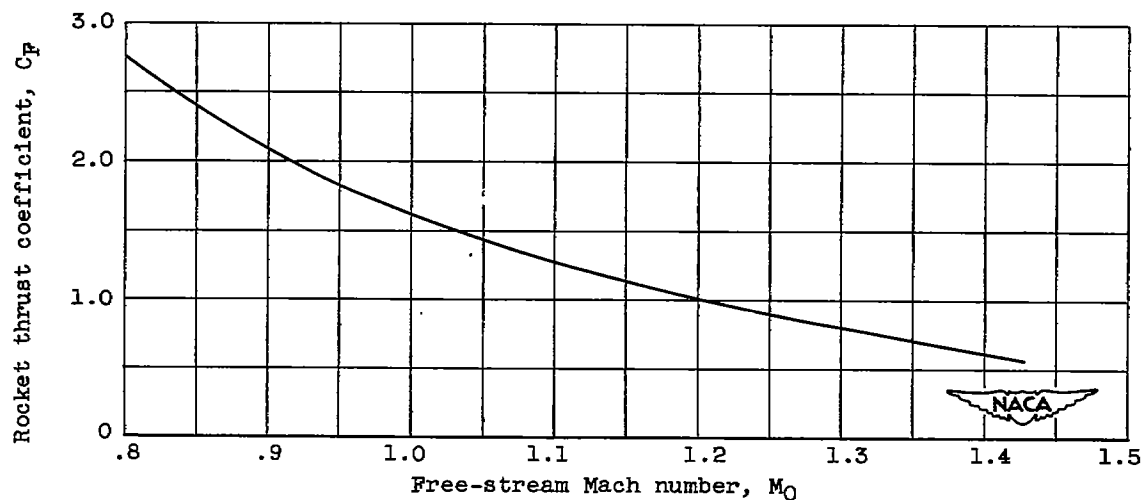


Figure 22. - Effect of free-stream Mach number on rocket thrust coefficient as based on performance data from reference 8.



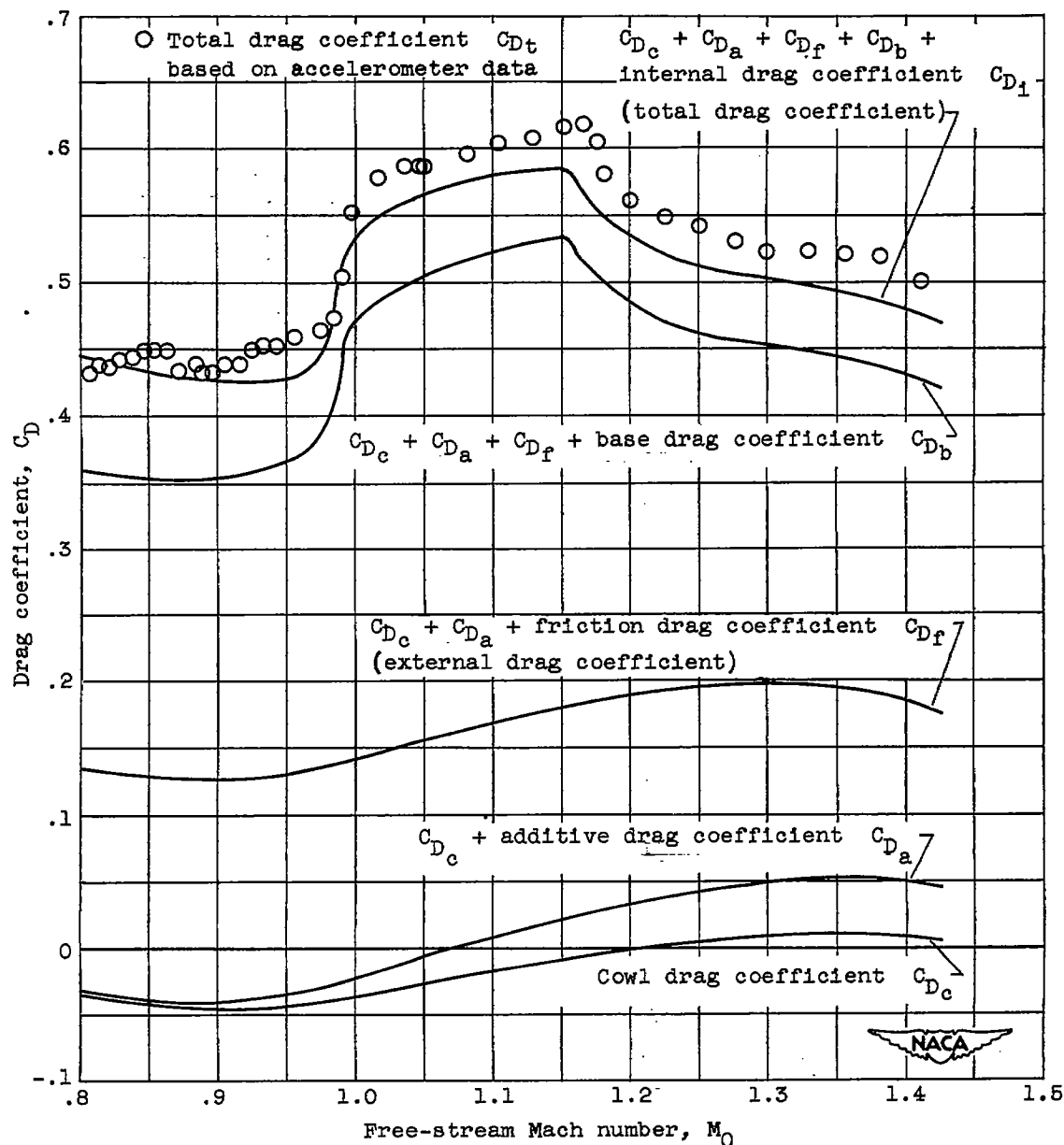


Figure 23. - Effect of free-stream Mach number on total drag coefficient and its component drag coefficients for rocket-off condition ( $0.750 \leq m/m_0 \leq 0.836$ ).

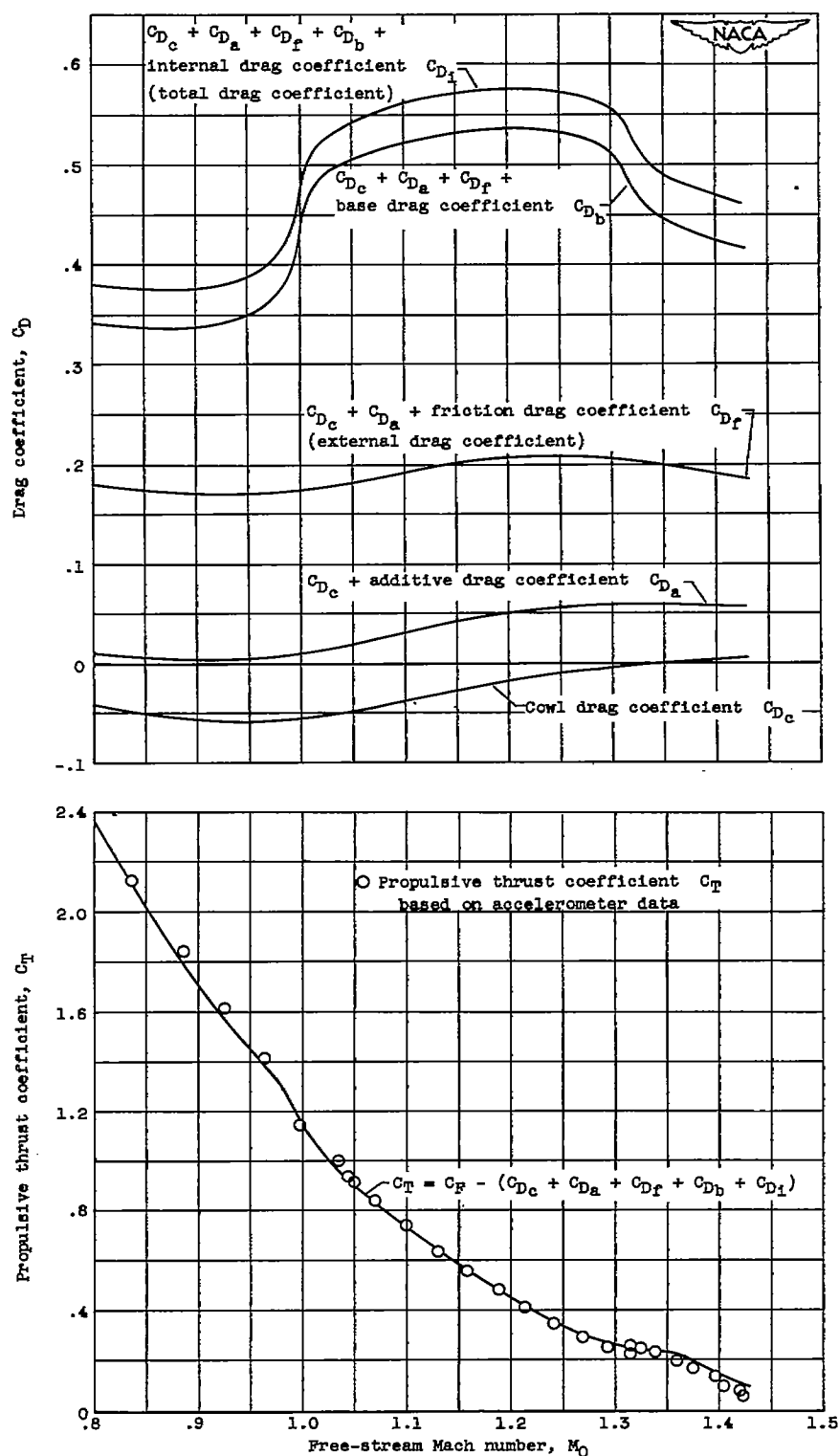


Figure 24. - Effect of free-stream Mach number on total drag coefficient and its component drag coefficients and propulsive thrust coefficient for rocket-on condition ( $0.665 \leq m/m_0 \leq 0.825$ ).

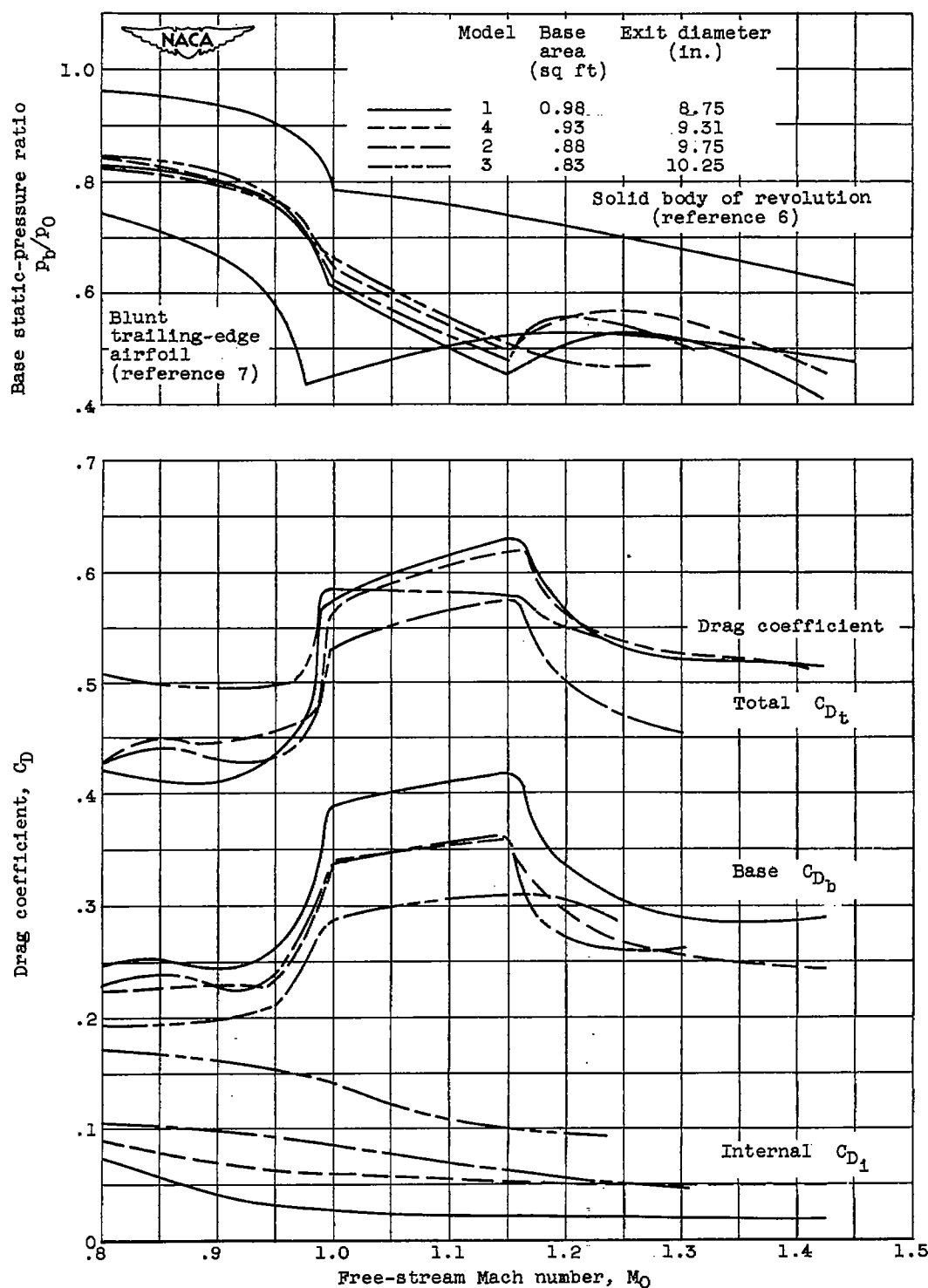


Figure 25. - Effect of free-stream Mach number on base static-pressure ratio and total, base, and internal drag coefficients for models 1, 2, 3, and 4 operating at rocket-off condition.